In-Situ and Operando Observation of Zinc Moss Growth and Dissolution in Alkaline Electrolyte for Zinc-Air Batteries

Yavuz Savsatli¹, Fan Wang¹, Hua Guo¹, Zeyuan Li¹, Andrew Hitt¹, Haizhou Zhan¹, Mingyuan Ge², Xianghui Xiao², Wah-Keat Lee², Harsh Agarwal³, Ryan M. Stephens³, Ming Tang^{1*}

- Department of Materials Science & NanoEngineering, Rice University, Houston, TX 77005,
 USA
- National Synchrotron Light Source II, Brookhaven National Laboratory, Upton, NY 11973, USA
- 3. Shell International Exploration and Production Inc., Houston, TX 77082, USA

^{*}Corresponding author email: mingtang@rice.edu

Abstract

As a promising battery technology, zinc-air batteries still face significant challenges, including the formation of mossy structure on the zinc metal anode in alkaline electrolyte. Because similar phenomenon also plagues lithium and sodium metal batteries, elucidating its mechanism has important implications for progress in energy storage. Herein, operando X-ray nanotomography was employed to visualize zinc moss growth and dissolution at the individual colony level. By tracking its microstructure evolution, zinc moss was found to display irreversible plating/stripping behavior. While zinc moss exhibits self-limiting growth and zinc deposition occurs mainly in its outer region, zinc dissolution is more uniformly distributed inside the moss colony upon stripping, leading to the formation of "dead" zinc and capacity loss. A direct correlation is established between the moss amount and zinc plating/stripping efficiency. Results from this study offer new insights into mitigating unstable zinc plating morphology and improving the cycle life of aqueous zinc-air batteries.

The widespread utilization of renewable energy to combat climate challenges depends on the development of advanced energy storage systems, particularly batteries with lower cost, higher energy densities, longer cycle life, and improved safety^{1–3}. The current lithium-ion battery (LIB) technology has made considerable progress in these aspects in the last several decades, but still faces challenges to meet the demanding requirements for its predominant adoption in electrical vehicles and electrical grid energy storage ^{4–6}. Rechargeable battery systems based on metallic anodes including lithium and zinc have received tremendous interest because of their significantly higher electrode specific capacities (Li: 3861 mAh g⁻¹, Zn: 820 mAh g⁻¹) over the ubiquitous graphite anode (338 mAh g⁻¹) in today's LIBs ^{7,8}. While batteries that use lithium metal electrodes, such as lithium sulfur and all solid-state lithium batteries, have attracted most of the attention, the raw materials cost and safety performance motivate research on Zn-based batteries such as Zn-ion and Zn-air batteries as well. Compared to lithium, zinc is more compatible with aqueous electrolytes, which facilitates the development of low-cost, safe and environment-friendly batteries that also offer high energy density^{9–12}.

Similar to lithium metal, however, the commercial viability of zinc aqueous rechargeable batteries is hindered by the low plating/stripping efficiency of the zinc metal electrode, caused by parasitic reactions such as hydrogen evolution. Recent research progress has resulted in considerable improvement in zinc metal's cycling stability in acidic electrolytes through judicious design of electrolyte, electrolyte additive, protective layer and substrate. Cao et al. report that the addition of an alkylammonium salt additive to a dilute acidic Zn(OTF)₂ electrolyte promotes the formation of a Zn²⁺-conducting and waterproof solid electrolyte interphase (SEI) layer, which raises the coulombic efficiency (CE) to 99.9% at 0.5 mA/cm² ¹³⁻¹⁶. Jiang et al. designed a

concentrated aqueous electrolyte containing 30 M ZnCl₂ + 5 M LiCl + 10 M TMACl which further increases CE to 99.6% at 0.2 mA/cm^2 ¹⁷.

While acidic electrolytes are mainly used in zinc ion batteries, alkaline electrolytes are the predominant choice of electrolytes for zinc-air batteries. In contrast to the recent development in acidic electrolytes, zinc plating/stipping efficiency in alkaline electrolytes remains low (<70%) ^{14,18}, which is closely related to the unfavorable morphologies exhibited by zinc deposits. In addition to the classic dendritic structure that primarily forms at relatively high current densities due to mass transport limitation, plating at lower current densities frequently leads to the formation of the mossy structure, which is also common during the electroplating of lithium and sodium. The mossy structure can be characterized as a cluster of intertwined and interconnected filaments or whiskers (Fig. 1), with filament diameters ranging between 50 and 200 nm in zinc ^{19,20}. Under moss-forming conditions, zinc in alkaline electrolytes typically demonstrates an initial period of layer-by-layer growth in the [0002] orientation (Fig. 1a), resulting hexagonal plate-like morphology on the substrate. It is then followed by the nucleation of small non-[0002]-oriented crystals on (0002) zinc surface (Fig. 1b) that undergo rapid filamentous growth (Fig. 1c). These filaments develop repeated kinks and branches during growth, ultimately evolving into a moss colony, and many of these colonies form separately on top of the compact zinc crystals (Fig. 1d).

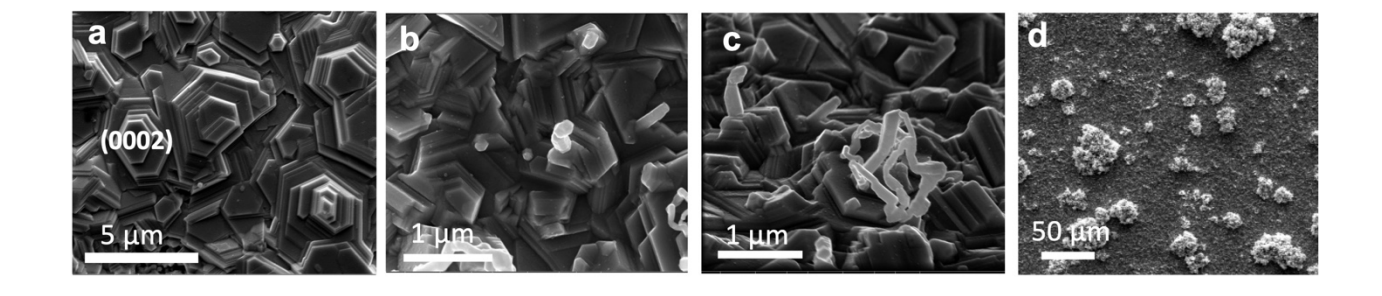


Figure 1. Morphological progression of zinc electrodeposits on the Cu substrate in alkaline electrolytes. **a)** Initial layer-by-layer zinc deposition in the [0002] direction. **b)** Nucleation of small crystallites with non-[0002] orientation on (0002) facets, serving as precursors to filamentous growth. **c)** Rapid growth of filaments along non-[0002], fast-growth directions. **d)** The evolution of zinc filaments into moss colonies through kinking and branching processes.

Though moss formation on lithium metallic anode is long known to be detrimental to its cycling stability and has been extensively studied, similar phenomenon in zinc aqueous batteries did not receive as much attention. Compared to dendritic growth, moss growth is equally if not more relevant to the application of zinc rechargeable batteries because it occurs at current densities commonly encountered in battery operation. While various methods have been developed to mitigate dendritic growth on zinc surface, e.g. by tailoring substrate structure and pulse plating, there is still a lack of effective strategies to suppress zinc moss in alkaline electrolytes, which highlights the need for a fundamental understanding of the zinc moss nucleation, growth and dissolution process ^{13,21}. A comparison of the moss structure evolution on zinc and alkaline metallic electrodes will also offer valuable insights into the moss formation mechanisms and the important factors that regulate its growth and dissolution process.

In recent years, in-situ and/or operando characterization techniques have been increasingly employed to improve the understanding of battery systems by tracking the evolution of their internal structure and chemistry in real time ^{22–30}. Specific to zinc electrodes, X-ray computed microtomography (microCT) was recently utilized in several studies to reveal important details of the zinc dendrite growth and dissolution process through 3D structure construction at microscale resolution in a non-destructive manner ^{31–33}. Qian et al. performed in-situ/operando X-ray

microscopy to visualize the Zinc plating and stripping behaviors in the acidic ZnSO₂ electrolyte and reveal that the substrate curvature and surface chemistry could have a significant effect on the zinc plating morphology³³. Utilizing a lab-based microCT system, Du et al. observed the nucleation and growth of zinc dendrites in ZnSO₄ electrolyte and the evolution of "dead" zinc particles during stripping. To our best knowledge, however, the growth and dissolution of the zinc moss structure in alkaline electrolytes has not yet been examined in details by advanced characterization techniques other than operando optical microscopy with microscale resolution ³⁴. For instance, Khezri et al. studied the effect of current density and flow rate on the electroplated zinc morphology and the bubble formation in zinc-air flow batteries with in-situ optical imaging³⁵. The nanoscale feature size of zinc moss presents challenges for microCT to probe its important structure characteristics.

In this work, operando X-ray nanotomography is employed to characterize the internal microstructure of zinc moss and its nucleation, growth and dissolution at the single colony level. By leveraging the bright monochromatic X-ray and X-ray optics at the Fast X-ray Imaging (FXI) beamline at the National Synchrotron Light Source II (NSLS-II), we track the morphology and internal porosity of individual moss colonies with both high spatial (sub-100 nm) and temporal (<2 minutes per scan) resolutions^{36,37}. Our experiment yields several notable findings. Moss growth is found to exhibit self-limiting behavior and stagnates at large moss volume while smaller moss colonies are favored to grow. We also observe significantly different distributions of the zinc plating vs. stripping flux inside the moss. While zinc deposition is concentrated in the outer region of the moss colony during plating, zinc stripping occurs much more homogeneously inside the moss. Such uniform zinc dissolution results in the collapse of the moss structure, causing it to be electrically disconnected from the substrate and become "dead" zinc. A positive correlation is

observed between the moss colony size and the zinc plating/stripping efficiency. These insights point to the importance of eliminating moss growth and controlling its stripping behavior for improving the cyclability of zinc metal electrodes. Guided by the mechanistic understanding, we uncovered that pulse plating could effectively suppress zinc moss growth by passivating the filament tips. Our study also demonstrates the value of operando X-ray nanotomography in advancing the battery science and technology.

Mossy structure evolution during electroplating

We first studied the zinc electroplating process in (6M KOH + 0.5M ZnO) aqueous electrolyte using the operando nanotomography setup as illustrated in Supplementary Fig. 1a. Our in-situ cell is made of an electrolyte-filled Kapton tube with copper and zinc wires inserted from the two opposite ends. The copper wire serves as the plating substrate, and the zinc wire was used as the counter electrode. We note that zinc deposits exhibit similar morphology on the Cu and Zn substrates. The copper wire was used as the working electrode instead of the zinc wire to avoid its potential dissolution during the stripping process. During the experiment, a constant potential of 0.05 V was applied between the two electrodes to plate zinc onto the tip region of the Cu wire while the sample was rotated to collect the x-ray projection images at a speed of two minutes per scan. As shown in Supplementary Fig. 1b, the plating current remained constant after an initial transient spike, indicating that ionic transport in the electrolyte reached a steady state. The average current density passing through the electrolyte was estimated to be 0.71 mA/cm² by dividing the current with the cross section area of the tube. Ex-situ zinc plating experiment shows that zinc moss grows on Cu substrate at such current density.

During nanotomographic measurement, the tip of the Cu wire was placed within the field of view to observe the plated Zn morphology in this region. We estimated the mass of zinc metal

deposited in the field of view from the segmented tomography images and found it to increase linearly with time (Supplementary Fig. 1c), which shows that zinc deposition also reached a steady state locally. Fig. 2 presents the reconstructed Zn deposits and Cu substrate viewed from three angles at different times of the plating process. The formation of the first moss colony (moss A, top row, blue region) on the substrate was observed at ~14 minutes after plating commenced. This is consistent with the existence of an "incubation period" for moss nucleation reported in earlier studies ³⁴. Two additional moss colonies (moss B and C, middle and bottom rows, blue regions) emerged on the Cu substrate between 14 and 22 minutes. The original nucleation sites of these moss colonies are marked by red circles in Fig. 2. They grew and merged with each other at later times. We applied the watershed algorithm to separate and visualize them individually in Fig. 2 to track their respective evolution. The moss colonies appears to grow isotropically in space and do not show preferential growth directions, which agrees with the moss morphology seen in SEM images (Fig. 1) and differs from the highly anisotropic morphology of zinc dendrites ³⁸. Such isotropic growth behavior is apparently facilitated by the frequent kinks developed on the zinc filaments, which change the filament growth direction.

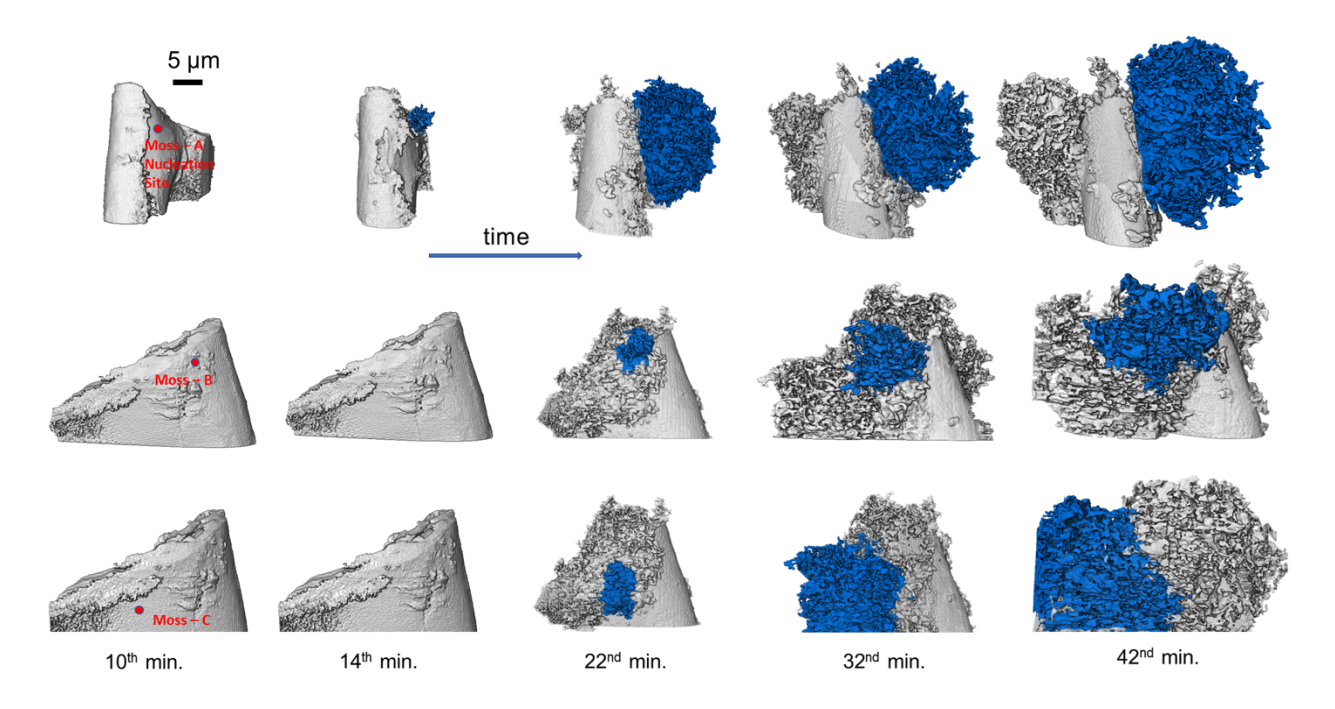


Figure 2. Nucleation and growth of three zinc moss colonies on Cu substrate during constant voltage plating. 3D rendering of zinc deposits plated on the Cu wire tip is reconstructed from operando nanotomography and viewed in different directions. Three zinc moss colonies (A, B and C) are highlighted by the blue color and visualized separately in the top, middle and bottom rows, respectively. The nucleation spots of the moss colonies are marked by red circles.

Fig. 3a shows the volumes of Moss A, B and C as a function of plating time. Moss A, which nucleated the first, had the largest growth rate among the three colonies at the early stage. However, its expansion stagnated around ~30 minutes after plating when Moss B and C nucleated and grew at faster rates during the same time. Even though the growth speeds of the individual colonies varied with time, the total moss volume increased at a constant rate throughout the plating process. This suggests that there is a competition between moss colonies for a constant incoming zinc flux, which was controlled by electrolyte transport. The slowdown of Moss A's growth in the presence of smaller Moss B and C implies that the larger moss colonies attract smaller zinc plating fluxes,

which is likely due to the decrease in the local driving force for zinc plating with increasing moss size. Growth of the moss structure is commonly believed to be surface reaction limited rather than diffusion limited. According to the Butler-Volmer equation, the zinc plating flux is controlled by the surface overpotential $\eta = V - \Delta \Phi_e - \Delta \Phi_i$, where V is the applied voltage between the working and counter electrodes (0.05 V in our experiment), $\Delta\Phi_i$ is the potential drop due to the ionic resistance in the electrolyte and $\Delta\Phi_e$ is the potential drop due to the electronic resistance in the solid phase. $\Delta\Phi_e$ increases with the moss volume because of the longer distance electrons need to travel from the Cu substrate along the zinc filaments to reach the growth front. This results in a lower η in larger moss colonies, which slows down their growth and gives away zinc flux to smaller colonies. Larger moss colonies may also induce a higher $\Delta\Phi_i$ because of the increased ion diffusion distance into the porous mossy structure. As will be discussed below, however, we discovered that zinc is predominantly deposited in the outer region of the moss colony during plating. Therefore, change in $\Delta\Phi_i$ should be relatively small compared to $\Delta\Phi_e$. Our observation provides evidence that zinc moss growth is self-limiting. Such behavior would promote the continuous nucleation of new moss colonies during zinc plating.

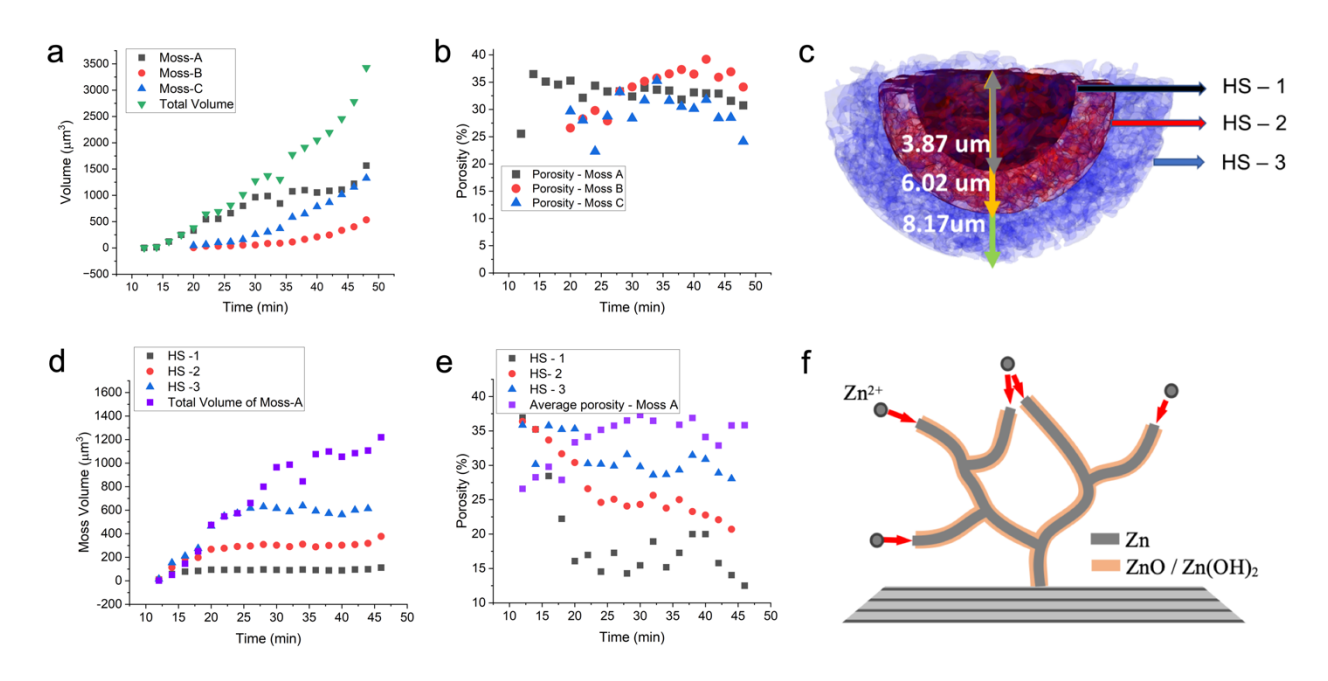


Figure 3. Quantitative analysis of moss volume and porosity evolution during zinc plating. a)

Total and individual moss volumes (excluding internal pore volume) versus plating time. **b)** Internal porosity of the mossy colonies versus time. **c)** Illustration of three concentric hemispheres (HS-1, HS-2, HS-3) surrounding Moss A, which are used to analyze the spatial variation of the zinc mass and pore volume inside the moss. **d,e)** Evolution of zinc volume and porosity within HS-1, HS-2, HS-3 and the entire Moss A. **f)** Schematic representation illustrating the progressive growth of mossy zinc at the tip of the structure.

While zinc moss is known to consist of entangled nanoscale filaments, its internal microstructure has not been examined in detail as per our knowledge. Although the spatial resolution of the transmission X-ray microscope employed in this study (80 nm) is not sufficient for resolving individual zinc filaments, the technique allows us to probe aggregated properties of the mossy structure such as its internal porosity based on the absorption contrast difference between zinc and electrolyte. Fig. 3b shows the porosity of Moss A, B and C as a function of time calculated from the operando tomographic dataset. Notably, the three moss colonies have a similar porosity

between 30% and 40% and the porosity value does not vary significantly with time during plating. We additionally reconstructed 10 moss colonies from the ex-situ tomography datasets of 3 different samples, which were electroplated at the same condition. While these moss colonies have a large size variation between 500 and 6000 μ m³, their porosity values are consistently in the range of 30%-45% with an average of 41% (see Supplementary Fig. 2), which confirms the statistical representativeness of the in-situ observation.

To confirm the porosity value determined from tomography, we also used focused ion beam/scanning electron microscopy (FIB/SEM) to reconstruct the moss 3D structure and measure its porosity. Supplementary Fig. 3a-c shows the SEM images of a zinc moss before and during FIB sectioning. Its reconstructed structure is shown in Supplementary Fig. 3d. FIB/SEM reconstruction is able to reveal the detailed filamentary structure inside the zinc moss due to the higher spatial resolution; however, the evolution of the mossy structure is not tracked due to the destructive nature of the technique. The internal porosity of the moss colony characterized by FIB/SEM is found to be 42%, which is very close to the value calculated from nanotomography. The operando observation that moss colonies maintain a relatively constant porosity during zinc plating indicates that their microstructure evolution eventually attains a steady state. Such behavior corroborates that moss growth at the colony level is controlled by surface reaction instead of mass transport kinetics as the latter usually results in microstructure coarsening, e.g. change in the porosity.

Taking advantage of the temporal information in the operando dataset, we analyzed the distribution of the zinc deposition flux within a moss colony to gain insights on its growth process. As illustrated in Fig. 3c, the space surrounding Moss A was partitioned by three concentric hemispheres (radii = 3.87, 6.02 and 8.17 μ m), the center of which is located at the moss nucleation site on the substrate. The amount of deposited zinc within each hemisphere was tracked

individually during plating as shown in Fig. 3d. The zinc volume in the smallest hemisphere (HS-1) first started to increase but saturated after c.a. 15 minutes of plating while it continued to increasing within the second hemisphere (HS-2). Similarly, zinc mass stopped growing within HS-2 after ~20 minutes of plating but kept increasing inside the largest hemisphere (HS-3), which eventually stagnated after ~25 minutes. Moss B and C also demonstrate similar trends (Supplementary Figure 4). This observed behavior suggests that the Zn was not uniformly deposited within the moss colony but mainly added to its outer region. The zinc plating flux vanishes in the moss interior, which explains why zinc mass inside each hemisphere eventually stopped increasing as the moss grew. Fig. 3e and Supplementary Fig. 4b,d show that the moss colonies become more porous as they grow. While the inner core (HS-1) has a relatively low porosity (<20%), the average porosity inside a dividing hemisphere increases with the hemisphere radius and approaches a steady value.

Given the above observation, it is highly likely that zinc is predominantly deposited onto the filament tip region during moss growth. When filaments extend in length, their tips gradually move away from the moss nucleation sites and shift the zinc deposit flux to the outer region. We postulate that the formation of a thin ZnO / Zn(OH)₂ layer on zinc surface, which is known for zinc electrodeposited in alkaline electrolyte, is responsible for the non-uniform zinc deposition onto the filaments. We characterized the passivation layer surrounding the zinc filaments by TEM to be about 5-10 nm thick and highly crystalline in nature (Supplementary Fig. 5). When such a dense layer forms on filament surface during plating, a large overpotential is required for zinc ions from the electrolyte to migrate across the layer, which limits the lateral growth of the filaments. However, the filament tips could be protected against passivation by the continuous zinc influx. When the deposition time of one atomic layer of zinc is shorter than the characteristic time of the

surface reaction kinetics, the exposed tip surface will be buried by newly arrived zinc atoms before being oxidized by the electrolyte. Upon reaching a dynamically steady state, the filament tips remain unpassivated and thus attract the majority of the zinc flux, resulting stable 1D filamentary growth. Fig. 3f illustrates this tip-growth mode of the zinc mossy structure.

Mossy structure evolution during electrostripping

We also investigated the morphological evolution of Zn mossy structure during the electrostripping process. Before the commencement of operando observation, zinc was electroplated onto the tip of copper wire at a voltage of +0.05 V (Cu/Zn) for 30 minutes in the insitu cell. After a brief rest, a reverse voltage of -0.05 V was applied to strip Zn from the Cu electrode concurrent with the tomographic measurement. The 3D reconstruction (Fig. 4) shows a large zinc moss located at the tip of the copper wire, which gradually shrank when stripping started. As shown in Fig. 5a, the zinc volume in this moss initially decreased at an approximately constant rate, but stopped changing after c.a. 5 minutes of stripping and became electrochemically inactive despite the constant voltage applied to the in-situ cell. The remaining "dead moss" accounts for about 30% of the zinc mass at the beginning of the stripping process.

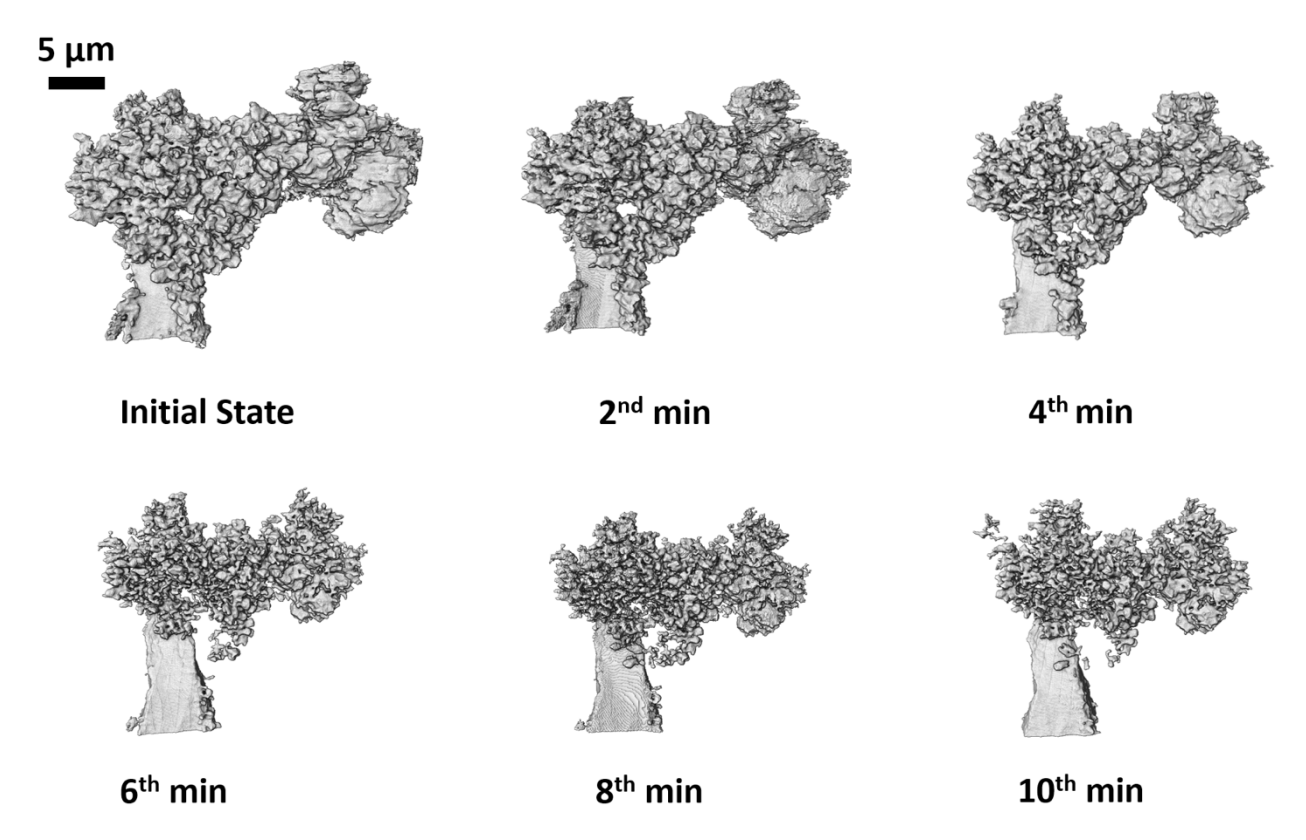


Figure 4. Dissolution of a zinc moss during constant voltage stripping. The zinc moss was grown at the tip of a copper wire by electroplating inside the in-situ cell, and its structure was reconstructed from operando nanotomography.

Upon analyzing the operando data, we discovered that the dissolution of zinc moss exhibits an important difference from its growth behavior, that is, the average internal porosity of the moss colony steadily increased from 35% to 57% during stripping (Fig. 5a) as against remaining constant during plating. This is a strong indication that zinc was removed from the moss interior, not just the outskirts as in the plating process. To further study the spatial distribution of the stripping flux, we divided the moss colony into the inner and exterior regions as illustrated in Fig. 5b. The inner region (solid blue) is a sphere of 13 µm in radius, which encompasses the core of the moss structure, and the exterior region consists of the rest of the moss volume. As shown in Fig.

5c, zinc mass was removed from these two regions at very similar rates, suggesting that zinc stripping took place quite uniformly within the mossy structure. In addition, close examination of the reconstructed moss colony reveals that part of the moss structure underwent rigid body movement during stripping. For example, Fig. 5d shows that the external features marked by the red boxes translated in space over the course of several minutes while retaining their morphologies. This is a sure sign of the internal contraction or even collapse of the moss due to zinc removal from its interior.

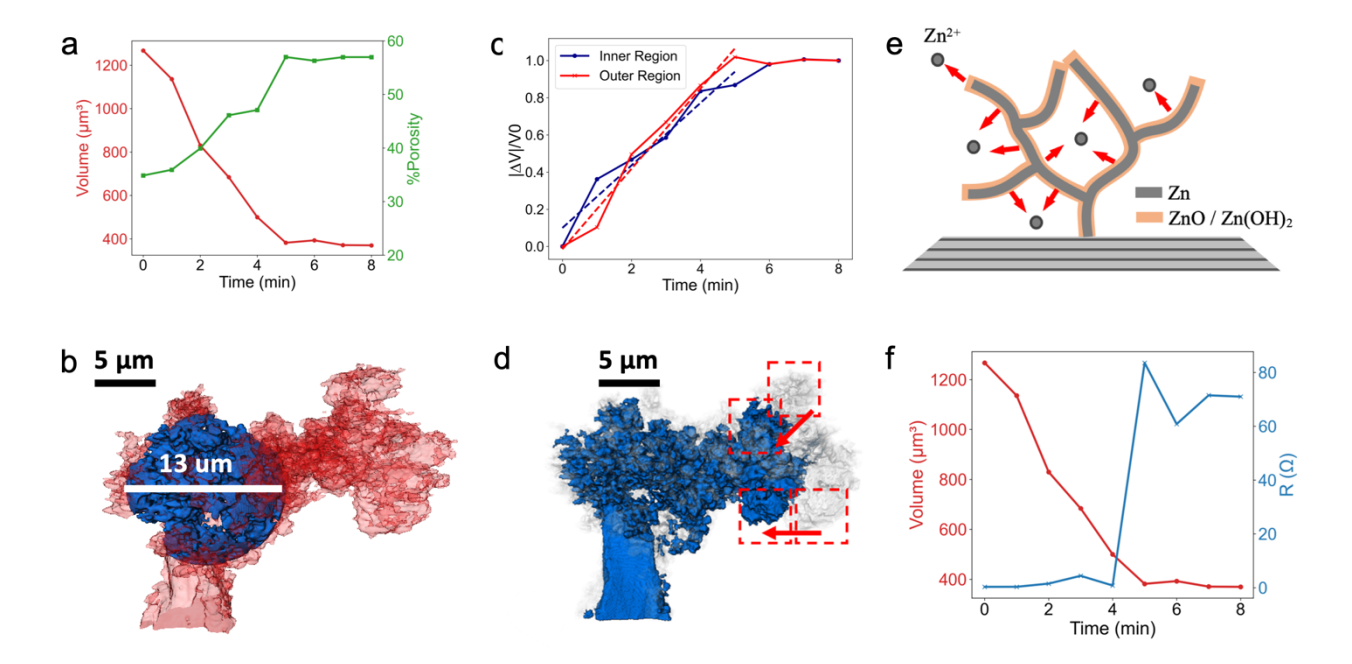


Figure 5. Analysis of moss dissolution behavior during electrostripping. a) Temporal evolution of the imaged moss volume (red line) and its internal porosity (green line). The moss structure stopped changing after 5 minutes of electrostripping. b) Visualization of the division of the moss structure into the inner (blue) and exterior (semitransparent red) regions. c) Fractions of the zinc mass removed from the inner and outer regions of the moss colony as a function of time. d) Reconstructed zinc moss (blue) after 8 minutes of electrostripping superimposed onto the initial moss structure (semitransparent gray). The red boxes and arrows highlight the morphology-preserving movement of two external moss features during the dissolution process. e) Schematics

of the zinc filament dissolution behavior upon electrostripping. **f)** Temporal evolution of the electrical resistance of the zinc moss, which is calculated based on the digital moss structure from tomographic reconstruction (see Methods in Supplementary Information). The resistance increased sharply when the moss volume (red line) stopped decreasing, indicating that the electrical disconnection of the moss from the substrate caused it to become electrochemically inactive.

Our operando study clearly reveals that the dissolution of a moss colony is not a simple reversal of its growth process. The passivation of the zinc filament tips offers a plausible explanation for this irreversible dissolution behavior. After the termination of zinc plating, the filament tips in the mossy structure are not protected by the zinc deposition flux anymore and will be passivated by reactions with the electrolyte. Therefore, the ZnO/Zn(OH)₄-covered tip region is no longer a preferential location for zinc removal during the stripping process. Accordingly, the zinc stripping flux would spread more uniformly along the filaments, which results in the dissolution of zinc atoms from the moss interior as illustrated in Fig. 5e. Additionally, the electrical resistance of the filaments reduces the stripping overpotential in the outer region of the moss and could further favor zinc dissolution inside the moss.

The presence of the stripping flux within the mossy structure has important consequence for its plating/stripping reversibility. Zinc dissolution from the side surfaces causes the thinning of filaments, which could break at weak spots such as sections that are relatively thin or covered by a defective passivation layer. The filament segments disconnected from the substrate become unstrippable because of the loss of electron conduction path. This could explain why the moss observed in our operando experiment did not completely dissolve. To add support to this

proposition, we used the reconstructed moss structure to compute its electrical resistance (see Methods in Supplementary Information). Fig. 5f shows that the moss resistance increased abruptly by two orders of magnitude at the same time when the stripping flux vanished corroborating the role of stripping-induced filament breaking and the resultant structure collapse in impeding moss dissolution.

The observed dead moss formation highlights the detrimental effect of the mossy structure on the cycling efficiency of zinc electrode. This was demonstrated in a series of galvanostatic zinc plating/stripping experiments, in which we assessed the correlation between the cycling efficiency and the extent of mossy growth in the zinc deposit. In the experiments, zinc was plated on a sputtered Cu substrate at a constant current of 5 mA/cm² for different amount of time (300, 400, 500 and 600 seconds) in the alkaline electrolyte, followed by stripping at 0.5 mA/cm² until reaching the cutoff voltage of -0.4 V. A smaller stripping current density was used here to facilitate the more reversible dissolution of the compact zinc crystals, which makes it easier to isolate the impact of zinc moss on the cycling stability. Fig. 6a shows that when the plating time was below 300 s, zinc deposit was largely free of moss growth. Increasing the plating time to 400, 500 and 600 s results in increasingly more moss colonies (Fig. 6b-d) with an estimated area coverage of ~5%, ~21.5% and ~41%, respectively. Correspondingly, the Coulombic efficiency (CE), which is calculated as the ratio of the stripping and plating capacities, drops significantly with the increase of the plating time (Fig. 6e). The average CE of the first 10 cycles (excluding the first cycle) is 81.3%, 78.22%, 75.80% and 67.30% for 300, 400, 500 and 600 s of plating, respectively. The low CE in the presence of a high density of moss colonies agrees with our in-situ observation showing that a significant fraction of zinc moss could not be stripped.

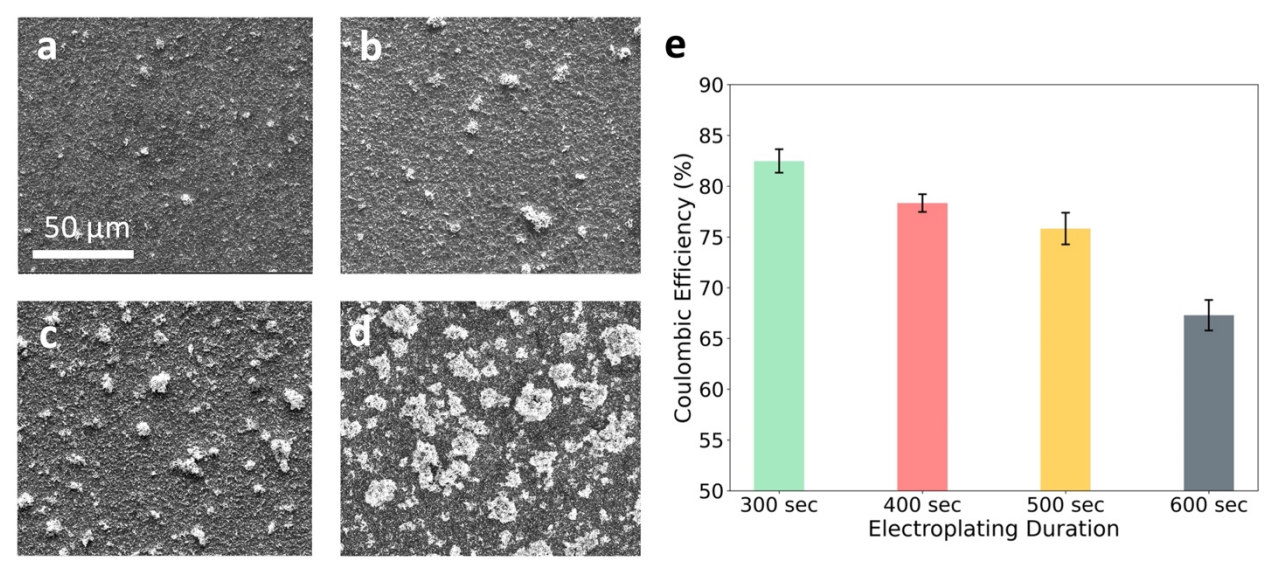


Figure 6. Correlation between the moss content and the plating/stripping efficiency of zinc metal electrode in alkaline electrolyte. a-d) SEM images of zinc deposit on copper substrate after 300, 400, 500 and 600 seconds of electroplating, where the mossy region appears lighter than compact zinc crystals. **e)** Effect of the electroplating time on the average Coulombic efficiency of the first 10 zinc plating/stripping cycles conducted with a plating current density of 5 mA/cm² and a stripping current density of 0.5 mA/cm².

Insights gained from this study also sheds useful light on promising ways to suppress zinc mossy growth. Our in-situ observation implies that zinc filament tips are prevented from passivation during plating due to the continuous incoming zinc flux (Fig. 3f), which causes zinc to be preferentially deposited onto the tip region that leads to sustained filament growth. This suggests that interrupting the zinc flux, e.g. via a pulse plating process, could potentially slow down or even stop the elongation of the zinc filaments by passivating their tips. To test this hypothesis, we plated zinc onto the Cu substrate with repeated current "ON/OFF" periods using a similar setup as in the galvanostatic zinc plating/stripping experiments. The plating current density is 5 mA/cm² in the ON period and 0 mA/cm² in the OFF period. Compared to constant current plating at 5 mA/cm², Supplementary Fig. 6 shows that the amount of zinc moss is substantially reduced upon pulse plating with 1 second of current ON and 0.5 second of current OFF, and the zinc deposits essentially become moss-free when the current OFF period is further increased to 1

second. A more comprehensive study of the effect of pulse plating on eliminating the moss structure and stabilizing the zinc electrode in alkaline electrolyte will be reported elsewhere.

While providing high spatial resolution, the restricted field of view afforded by the operando nanotomography technique limits the observation to several moss colonies, which does not permit statistical analysis of the moss growth/dissolution behavior. The in-situ setup differs from the conventional battery configurations, and a relatively low current density was used to provide sufficient temporal resolution of the zinc plating/stripping process. These limitations need to be taken into consideration when interpreting the significance of the operando results for real battery applications. Nevertheless, we have shown that our observations elucidate the effect of mossy structure on the cycling stability of zinc metal electrodes and how pulse plating could suppress zinc moss growth at a practical current density, which provides confidence in the relevance of the operando study to zinc-air batteries.

As two promising metallic anodes for rechargeable batteries, both zinc and lithium undergo mossy growth during plating. While zinc and lithium mosses share many similarities, they also exhibit notable difference. Zinc filaments are much thinner (50 – 100 nm) than lithium whiskers formed in carbonate or ether electrolytes, whose diameters are in the range of 100 nm – 10 µm ^{39,40}. The different filament sizes could be attributed to their different surface passivation layer structures and surface reaction rates. Zinc filaments growing in alkaline electrolyte are covered by a dense, crystalline inorganic layer, which is difficult for large zinc ions to diffuse across limiting filament thickening. In contrast, the solid electrolyte interphase (SEI) layer formed on the lithium metal surface usually contains a mixture of inorganic and organic components, which is more permeable to the relatively small lithium ions ^{41,42}. As such, lithium filaments could continuously grow laterally during plating through lithium deposition onto the side surfaces, resulting in larger

diameters than zinc filaments. The increase of lithium filament size with Li diffusivity in SEI has been reported ³⁷. Moreover, the relatively high permeability of the lithium SEI layer allows lithium to be plated inside the mossy structure to induce moss expansion from within ⁴³, a phenomenon that is often likened to a "rising dough". In-situ optical and transmission electron microscopy observations show that lithium could be simultaneously deposited at the base, kinks and tips of the filaments ^{43–45}. In comparison, zinc deposition onto a moss colony is non-uniform and confined to its shell region. Despite their difference, mossy lithium has a similar internal porosity (c.a. 30-50%⁴⁶) as zinc moss as determined in this study. Like zinc moss, lithium moss colonies also display competitive growth among them under constant current plating conditions, with the growth of some colonies stagnating while others persist⁴³.

During stripping, both zinc and lithium suffer from the formation of dead moss due to stripping-induced filament thinning. For example, notched regions were observed to develop on Li filaments in EC/DEC electrolyte⁴⁷. The fast local lithium dissolution causes the filaments to pinch off and disconnect from the substrate, which is believed to be a major contributor to the capacity fade of lithium metal anode ⁴⁸. Similar phenomenon could happen to zinc filaments too, and their smaller diameters make it an even more serious problem for the cycling stability of zinc metal, which is evidenced by its low plating/stripping efficiency as measured in our experiments. Identifying effective strategies such as pulse plating to suppress moss growth in alkaline electrolyte is thus important for the development of long-cycle-life zinc-air batteries. Additionally, tailoring the surface passivation layer to make it more permeable to zinc transport would perceivably increase the filament size and reduce the likelihood of filament breaking upon stripping. This could also become a fruitful approach to improving the cyclability of the Zn metal electrode if moss growth could not be fully eliminated.

In summary, the morphological evolution of zinc mossy structure during plating and stripping in alkaline electrolyte was studied by the synchrotron-based operando nanotomographic technique to shed light on its growth and dissolution mechanisms. During Zn plating, zinc filaments nucleate on Cu substrate and grow into moss colonies that maintain a relatively constant internal porosity around 40%. Evidence was obtained that suggests zinc moss growth to be self-limiting because of the increased impedance with moss size. Our operando observation reveals the irreversibility of the zinc plating/stripping process. While zinc plating flux is concentrated in the outer region of the moss colonies, which is likely due to the preferential zinc deposition onto the filament tips, zinc dissolution occurs more uniformly inside the moss as a result of the passivation of filament tips. Such a change in the zinc flux distribution was found to make zinc filaments prone to fracture upon stripping, which leads to the formation of dead moss that significantly reduces the cycling efficiency of the zinc metal electrode.

Acknowledgements

Y.S., F.W., and M.T. acknowledge support from the Department of Energy, Basic Energy Sciences under project DE-SC0019111 (nanotomography of zinc plating) and Shell International Exploration and Production Inc (nanotomography of zinc stripping). Z.L. is supported by National Science Foundation under project CMMI-1929949. A.H. is supported by Air Force Office of Scientific Research through Grant No. FA9550-21-1-0460. Operando nanotomography experiments were performed at beamline 18-ID, National Synchrotron Light Source II, Brookhaven National Laboratory, which are supported by the U.S. DOE, Office of Science, Office of Basic Energy Sciences under Contract No. DE-AC02-98CH10886. COMSOL calculations were

performed on computing clusters at the Texas Advanced Computing Center (TACC) of The University of Texas.

Supporting Information available: additional experimental and modeling methods and details, including ex-situ tomography, FIB/SEM reconstruction and TEM images of the zinc mossy structure as well as SEM images of the pulse plated zinc morphology.

References

- (1) Zhan, R.; Wang, X.; Chen, Z.; Seh, Z. W.; Wang, L.; Sun, Y. Promises and Challenges of the Practical Implementation of Prelithiation in Lithium-Ion Batteries. *Advanced Energy Materials* **2021**, *11* (35), 2101565. https://doi.org/10.1002/aenm.202101565.
- (2) Wu, F.; Maier, J.; Yu, Y. Guidelines and Trends for Next-Generation Rechargeable Lithium and Lithium-Ion Batteries. *Chem. Soc. Rev.* **2020**, *49* (5), 1569–1614. https://doi.org/10.1039/C7CS00863E.
- (3) Luderer, G.; Madeddu, S.; Merfort, L.; Ueckerdt, F.; Pehl, M.; Pietzcker, R.; Rottoli, M.; Schreyer, F.; Bauer, N.; Baumstark, L.; Bertram, C.; Dirnaichner, A.; Humpenöder, F.; Levesque, A.; Popp, A.; Rodrigues, R.; Strefler, J.; Kriegler, E. Impact of Declining Renewable Energy Costs on Electrification in Low-Emission Scenarios. *Nat Energy* **2022**, 7 (1), 32–42. https://doi.org/10.1038/s41560-021-00937-z.
- (4) Zhang, S.; Li, Y.; Bannenberg, L. J.; Liu, M.; Ganapathy, S.; Wagemaker, M. The Lasting Impact of Formation Cycling on the Li-Ion Kinetics between SEI and the Li-Metal Anode and Its Correlation with Efficiency. *Science Advances* **2024**, *10* (3), eadj8889. https://doi.org/10.1126/sciadv.adj8889.
- (5) Xiang, Y.; Tao, M.; Zhong, G.; Liang, Z.; Zheng, G.; Huang, X.; Liu, X.; Jin, Y.; Xu, N.; Armand, M.; Zhang, J.-G.; Xu, K.; Fu, R.; Yang, Y. Quantitatively Analyzing the Failure Processes of Rechargeable Li Metal Batteries. *Science Advances* **2021**, *7* (46), eabj3423. https://doi.org/10.1126/sciadv.abj3423.
- (6) Li, A.-M.; Wang, Z.; Pollard, T. P.; Zhang, W.; Tan, S.; Li, T.; Jayawardana, C.; Liou, S.-C.; Rao, J.; Lucht, B. L.; Hu, E.; Yang, X.-Q.; Borodin, O.; Wang, C. High Voltage Electrolytes for Lithium-Ion Batteries with Micro-Sized Silicon Anodes. *Nat Commun* **2024**, *15* (1), 1206. https://doi.org/10.1038/s41467-024-45374-0.
- (7) Liu, J.; Bao, Z.; Cui, Y.; Dufek, E. J.; Goodenough, J. B.; Khalifah, P.; Li, Q.; Liaw, B. Y.; Liu, P.; Manthiram, A.; Meng, Y. S.; Subramanian, V. R.; Toney, M. F.; Viswanathan, V. V.; Whittingham, M. S.; Xiao, J.; Xu, W.; Yang, J.; Yang, X.-Q.; Zhang, J.-G. Pathways for Practical High-Energy Long-Cycling Lithium Metal Batteries. *Nat Energy* **2019**, *4* (3), 180–186. https://doi.org/10.1038/s41560-019-0338-x.
- (8) Zhang, H.; Wang, L.; Li, H.; He, X. Criterion for Identifying Anodes for Practically Accessible High-Energy-Density Lithium-Ion Batteries. *ACS Energy Lett.* **2021**, *6* (10), 3719–3724. https://doi.org/10.1021/acsenergylett.1c01713.
- (9) Advanced Extremely Durable 3D Bifunctional Air Electrodes for Rechargeable Zinc-Air Batteries Lee 2014 Advanced Energy Materials Wiley Online Library. https://onlinelibrary.wiley.com/doi/epdf/10.1002/aenm.201301389 (accessed 2024-03-17).
- (10) Wang, M.; Zhang, F.; Lee, C.-S.; Tang, Y. Low-Cost Metallic Anode Materials for High Performance Rechargeable Batteries. *Adv. Energy Mater.* **2017**, *7* (23), 1700536. https://doi.org/10.1002/aenm.201700536.
- (11) Kim, H.; Jeong, G.; Kim, Y.-U.; Kim, J.-H.; Park, C.-M.; Sohn, H.-J. Metallic Anodes for next Generation Secondary Batteries. *Chem. Soc. Rev.* **2013**, *42* (23), 9011–9034. https://doi.org/10.1039/C3CS60177C.
- (12) Han, C.; Li, W.; Liu, H. K.; Dou, S.; Wang, J. Principals and Strategies for Constructing a Highly Reversible Zinc Metal Anode in Aqueous Batteries. *Nano Energy* **2020**, *74*, 104880. https://doi.org/10.1016/j.nanoen.2020.104880.

- (13) Zheng, J.; Zhao, Q.; Tang, T.; Yin, J.; Quilty, C. D.; Renderos, G. D.; Liu, X.; Deng, Y.; Wang, L.; Bock, D. C.; Jaye, C.; Zhang, D.; Takeuchi, E. S.; Takeuchi, K. J.; Marschilok, A. C.; Archer, L. A. Reversible Epitaxial Electrodeposition of Metals in Battery Anodes. *Science* **2019**, *366* (6465), 645–648. https://doi.org/10.1126/science.aax6873.
- (14) Wang, F.; Borodin, O.; Gao, T.; Fan, X.; Sun, W.; Han, F.; Faraone, A.; Dura, J. A.; Xu, K.; Wang, C. Highly Reversible Zinc Metal Anode for Aqueous Batteries. *Nature Mater* **2018**, *17* (6), 543–549. https://doi.org/10.1038/s41563-018-0063-z.
- (15) Xu, W.; Zhao, K.; Huo, W.; Wang, Y.; Yao, G.; Gu, X.; Cheng, H.; Mai, L.; Hu, C.; Wang, X. Diethyl Ether as Self-Healing Electrolyte Additive Enabled Long-Life Rechargeable Aqueous Zinc Ion Batteries. *Nano Energy* **2019**, *62*, 275–281. https://doi.org/10.1016/j.nanoen.2019.05.042.
- (16) Cao, L.; Li, D.; Pollard, T.; Deng, T.; Zhang, B.; Yang, C.; Chen, L.; Vatamanu, J.; Hu, E.; Hourwitz, M. J.; Ma, L.; Ding, M.; Li, Q.; Hou, S.; Gaskell, K.; Fourkas, J. T.; Yang, X.-Q.; Xu, K.; Borodin, O.; Wang, C. Fluorinated Interphase Enables Reversible Aqueous Zinc Battery Chemistries. *Nat. Nanotechnol.* **2021**, *16* (8), 902–910. https://doi.org/10.1038/s41565-021-00905-4.
- (17) Jiang, H.; Tang, L.; Fu, Y.; Wang, S.; Sandstrom, S. K.; Scida, A. M.; Li, G.; Hoang, D.; Hong, J. J.; Chiu, N.-C.; Stylianou, K. C.; Stickle, W. F.; Wang, D.; Li, J.; Greaney, P. A.; Fang, C.; Ji, X. Chloride Electrolyte Enabled Practical Zinc Metal Battery with a Near-Unity Coulombic Efficiency. *Nat Sustain* **2023**, *6* (7), 806–815. https://doi.org/10.1038/s41893-023-01092-x.
- (18) Fu, J.; Cano, Z. P.; Park, M. G.; Yu, A.; Fowler, M.; Chen, Z. Electrically Rechargeable Zinc-Air Batteries: Progress, Challenges, and Perspectives. *Adv. Mater.* **2017**, *29* (7), 1604685. https://doi.org/10.1002/adma.201604685.
- (19) Wang, R. Y.; Kirk, D. W.; Zhang, G. X. Effects of Deposition Conditions on the Morphology of Zinc Deposits from Alkaline Zincate Solutions. *J. Electrochem. Soc.* **2006**, *153* (5), C357. https://doi.org/10.1149/1.2186037.
- (20) Wang, R. Y.; Kirk, D. W.; Zhang, G. X. Characterization and Growth Mechanism of Filamentous Zinc Electrodeposits. *ECS Trans.* **2007**, *2* (16), 19–27. https://doi.org/10.1149/1.2424307.
- (21) Wang, K.; Pei, P.; Ma, Z.; Chen, H.; Xu, H.; Chen, D.; Wang, X. Dendrite Growth in the Recharging Process of Zinc–Air Batteries. *J. Mater. Chem. A* **2015**, *3* (45), 22648–22655. https://doi.org/10.1039/C5TA06366C.
- (22) Du, W.; Zhang, Z.; Iacoviello, F.; Zhou, S.; Owen, R. E.; Jervis, R.; Brett, D. J. L.; Shearing, P. R. Observation of Zn Dendrite Growth via Operando Digital Microscopy and Time-Lapse Tomography. *ACS Appl. Mater. Interfaces* **2023**, acsami.2c19895. https://doi.org/10.1021/acsami.2c19895.
- (23) Lu, J.; Wu, T.; Amine, K. State-of-the-Art Characterization Techniques for Advanced Lithium-Ion Batteries. *Nat Energy* **2017**, *2* (3), 1–13. https://doi.org/10.1038/nenergy.2017.11.
- (24) Zhang, L.; Fan, H.; Dang, Y.; Zhuang, Q.; Arandiyan, H.; Wang, Y.; Cheng, N.; Sun, H.; Pérez Garza, H. H.; Zheng, R.; Wang, Z.; S Mofarah, S.; Koshy, P.; Bhargava, S. K.; Cui, Y.; Shao, Z.; Liu, Y. Recent Advances in in Situ and Operando Characterization Techniques for Li7La3Zr2O12-Based Solid-State Lithium Batteries. *Mater Horiz* **2023**, *10* (5), 1479–1538. https://doi.org/10.1039/d3mh00135k.

- (25) Strauss, F.; Kitsche, D.; Ma, Y.; Teo, J. H.; Goonetilleke, D.; Janek, J.; Bianchini, M.; Brezesinski, T. Operando Characterization Techniques for All-Solid-State Lithium-Ion Batteries. *Advanced Energy and Sustainability Research* **2021**, *2* (6), 2100004. https://doi.org/10.1002/aesr.202100004.
- (26) Liu, D.; Shadike, Z.; Lin, R.; Qian, K.; Li, H.; Li, K.; Wang, S.; Yu, Q.; Liu, M.; Ganapathy, S.; Qin, X.; Yang, Q.-H.; Wagemaker, M.; Kang, F.; Yang, X.-Q.; Li, B. Review of Recent Development of In Situ/Operando Characterization Techniques for Lithium Battery Research. *Advanced Materials* **2019**, *31* (28), 1806620. https://doi.org/10.1002/adma.201806620.
- (27) Wu, Y.; Liu, N. Visualizing Battery Reactions and Processes by Using *In Situ* and *In Operando* Microscopies. *Chem* **2018**, *4* (3), 438–465. https://doi.org/10.1016/j.chempr.2017.12.022.
- (28) Hou, D.; Xia, D.; Gabriel, E.; Russell, J. A.; Graff, K.; Ren, Y.; Sun, C.-J.; Lin, F.; Liu, Y.; Xiong, H. Spatial and Temporal Analysis of Sodium-Ion Batteries. *ACS Energy Lett.* **2021**, 6 (11), 4023–4054. https://doi.org/10.1021/acsenergylett.1c01868.
- (29) Zhang, Z.; Said, S.; Smith, K.; Jervis, R.; Howard, C. A.; Shearing, P. R.; Brett, D. J. L.; Miller, T. S. Characterizing Batteries by In Situ Electrochemical Atomic Force Microscopy: A Critical Review. *Advanced Energy Materials* **2021**, *11* (38), 2101518. https://doi.org/10.1002/aenm.202101518.
- (30) Wang, F.; Yang, K.; Ge, M.; Wang, J.; Wang, J.; Xiao, X.; Lee, W.-K.; Li, L.; Tang, M. Reaction Heterogeneity in LiFePO4 Agglomerates and the Role of Intercalation-Induced Stress. *ACS Energy Lett.* **2022**, *7* (5), 1648–1656. https://doi.org/10.1021/acsenergylett.2c00226.
- (31) Franke-Lang, R.; Arlt, T.; Manke, I.; Kowal, J. X-Ray Tomography as a Powerful Method for Zinc-Air Battery Research. *Journal of Power Sources* **2017**, *370*, 45–51. https://doi.org/10.1016/j.jpowsour.2017.10.010.
- (32) Yufit, V.; Tariq, F.; Eastwood, D. S.; Biton, M.; Wu, B.; Lee, P. D.; Brandon, N. P. Operando Visualization and Multi-Scale Tomography Studies of Dendrite Formation and Dissolution in Zinc Batteries. *Joule* **2019**, *3* (2), 485–502. https://doi.org/10.1016/j.joule.2018.11.002.
- (33) Qian, G.; Zan, G.; Li, J.; Lee, S.; Wang, Y.; Zhu, Y.; Gul, S.; Vine, D. J.; Lewis, S.; Yun, W.; Ma, Z.; Pianetta, P.; Lee, J.; Li, L.; Liu, Y. Structural, Dynamic, and Chemical Complexities in Zinc Anode of an Operating Aqueous Zn-Ion Battery. *Advanced Energy Materials* **2022**, *12* (21), 2200255. https://doi.org/10.1002/aenm.202200255.
- (34) Otani, T.; Nagata, M.; Fukunaka, Y.; Homma, T. Morphological Evolution of Mossy Structures during the Electrodeposition of Zinc from an Alkaline Zincate Solution. *Electrochimica Acta* **2016**, *206*, 366–373. https://doi.org/10.1016/j.electacta.2016.04.124.
- (35) Khezri, R.; Motlagh, S. R.; Etesami, M.; Mohamad, A. A.; Pornprasertsuk, R.; Olaru, S.; Kheawhom, S. High Current Density Charging of Zinc-Air Flow Batteries: Investigating the Impact of Flow Rate and Current Density on Zinc Electrodeposition. *Applied Energy* **2023**, *348*, 121564. https://doi.org/10.1016/j.apenergy.2023.121564.
- (36) Ge, M.; Coburn, D. S.; Nazaretski, E.; Xu, W.; Gofron, K.; Xu, H.; Yin, Z.; Lee, W.-K. One-Minute Nano-Tomography Using Hard X-Ray Full-Field Transmission Microscope. *Applied Physics Letters* **2018**, *113* (8), 083109. https://doi.org/10.1063/1.5048378.
- (37) Hitt, A.; Wang, F.; Li, Z.; Ge, M.; Zhang, Y.; Savsatli, Y.; Xiao, X.; Lee, W.-K.; Stephens, R.; Tang, M. Nanotomographic Observation and Statistical Analysis of Overcharging

- Induced Cracks in LiCoO2 Single Crystalline Particles. *Energy Storage Materials* **2022**, *52*, 320–328. https://doi.org/10.1016/j.ensm.2022.08.011.
- (38) Yuan, X.; He, C.; Wang, J.; You, X.; Chen, Y.; Gou, Q.; Yang, N.; Xie, G.; Hou, Y. Inhibition of Zinc Dendrite Growth in Zinc-Air Batteries by Alloying the Anode with Ce and Yb. *Journal of Alloys and Compounds* **2024**, *970*, 172523. https://doi.org/10.1016/j.jallcom.2023.172523.
- (39) Yu, S.-H.; Huang, X.; Brock, J. D.; Abruña, H. D. Regulating Key Variables and Visualizing Lithium Dendrite Growth: An Operando X-Ray Study. *J. Am. Chem. Soc.* **2019**, *141* (21), 8441–8449. https://doi.org/10.1021/jacs.8b13297.
- (40) Fang, S.; Zhang, Y.; Liu, X. Lithium Anode in Carbonate-Based Electrolyte: High-Performance by Self-Protected Solid-Electrolyte-Interphase. *Chemical Engineering Journal* **2021**, *426*, 131880. https://doi.org/10.1016/j.cej.2021.131880.
- (41) Chen, X.; Yao, Y.; Yan, C.; Zhang, R.; Cheng, X.; Zhang, Q. A Diffusion--Reaction Competition Mechanism to Tailor Lithium Deposition for Lithium-Metal Batteries. *Angew. Chem. Int. Ed.* **2020**, *59* (20), 7743–7747. https://doi.org/10.1002/anie.202000375.
- (42) Zheng, J. X. K.; Yin, J.; Tang, T.; Archer, L. A. Moss-like Growth of Metal Electrodes: On the Role of Competing Faradaic Reactions and Fast Charging. *ACS Energy Lett.* **2023**, *8* (5), 2113–2121. https://doi.org/10.1021/acsenergylett.3c00120.
- (43) Steiger, J.; Kramer, D.; Mönig, R. Microscopic Observations of the Formation, Growth and Shrinkage of Lithium Moss during Electrodeposition and Dissolution. *Electrochimica Acta* **2014**, *136*, 529–536. https://doi.org/10.1016/j.electacta.2014.05.120.
- (44) Kushima, A.; So, K. P.; Su, C.; Bai, P.; Kuriyama, N.; Maebashi, T.; Fujiwara, Y.; Bazant, M. Z.; Li, J. Liquid Cell Transmission Electron Microscopy Observation of Lithium Metal Growth and Dissolution: Root Growth, Dead Lithium and Lithium Flotsams. *Nano Energy* **2017**, *32*, 271–279. https://doi.org/10.1016/j.nanoen.2016.12.001.
- (45) Steiger, J.; Kramer, D.; Mönig, R. Mechanisms of Dendritic Growth Investigated by in Situ Light Microscopy during Electrodeposition and Dissolution of Lithium. *Journal of Power Sources* **2014**, *261*, 112–119. https://doi.org/10.1016/j.jpowsour.2014.03.029.
- (46) Cheng, J.-H.; Assegie, A. A.; Huang, C.-J.; Lin, M.-H.; Tripathi, A. M.; Wang, C.-C.; Tang, M.-T.; Song, Y.-F.; Su, W.-N.; Hwang, B. J. Visualization of Lithium Plating and Stripping via *in Operando* Transmission X-Ray Microscopy. *J. Phys. Chem. C* **2017**, *121* (14), 7761–7766. https://doi.org/10.1021/acs.jpcc.7b01414.
- (47) Li, Y.; Huang, W.; Li, Y.; Pei, A.; Boyle, D. T.; Cui, Y. Correlating Structure and Function of Battery Interphases at Atomic Resolution Using Cryoelectron Microscopy. *Joule* **2018**, *2* (10), 2167–2177. https://doi.org/10.1016/j.joule.2018.08.004.
- (48) Fang, C.; Li, J.; Zhang, M.; Zhang, Y.; Yang, F.; Lee, J. Z.; Lee, M.-H.; Alvarado, J.; Schroeder, M. A.; Yang, Y.; Lu, B.; Williams, N.; Ceja, M.; Yang, L.; Cai, M.; Gu, J.; Xu, K.; Wang, X.; Meng, Y. S. Quantifying Inactive Lithium in Lithium Metal Batteries. *Nature* **2019**, *572* (7770), 511–515. https://doi.org/10.1038/s41586-019-1481-z.

ToC Graphic

